

# Layer number and stacking order-dependent thermal transport in molybdenum disulfide with sulfur vacancies

Ranjuna M K\* and Jayakumar Balakrishnan†

*Department of Physics, Indian Institute of Technology Palakkad, Palakkad-678623, Kerala, India*

(Dated: July 26, 2023)

## Abstract

Recent theoretical works on two-dimensional molybdenum disulfide,  $\text{MoS}_2$ , with sulfur vacancies predict that the suppression of thermal transport in  $\text{MoS}_2$  by point defects is more prominent in monolayers and becomes negligible as layer number increases. Here, we investigate experimentally the thermal transport properties of two-dimensional molybdenum disulfide crystals with inherent sulfur vacancies. We study the first-order temperature coefficients of interlayer and intralayer Raman modes of  $\text{MoS}_2$  crystals with different layer numbers and stacking orders. The in-plane thermal conductivity ( $\kappa$ ) and total interface conductance per unit area ( $g$ ) across the 2D material-substrate interface of mono-, bi- and tri-layer  $\text{MoS}_2$  samples are measured using the micro-Raman thermometry. Our results clearly demonstrate that the thermal conductivity is significantly suppressed by sulfur vacancies in monolayer  $\text{MoS}_2$ . However, this reduction in  $\kappa$  becomes less evident as the layer number increases, confirming the theoretical predictions. No significant variation is observed in the  $\kappa$  and  $g$  values of 2H and 3R stacked bilayer  $\text{MoS}_2$  samples.

## INTRODUCTION

Two-dimensional transition metal dichalcogenides (TMDs), an advancing class of layered materials, have recently become a fertile ground for investigating fundamental properties and emergent device applications. Among these, 2D crystals of molybdenum disulfide ( $\text{MoS}_2$ ) have gained significant importance due to their unique properties, such as direct bandgap in monolayer[1], high carrier mobility, significant light-matter interactions[2], reasonable spin-orbit interactions[3], good valley selectivity[4–6] and high Seebeck coefficient[7–9]. This makes them potential materials for applications in electronics[10–12], optoelectronics[13–15], Valleytronics[4, 5, 16] and energy harvesting.[9, 17] However, the number and stacking order of layers and the defects and impurities in  $\text{MoS}_2$  can significantly impact its properties and the device’s performance.[18]

Monolayer  $\text{MoS}_2$  comprises the hexagonal arrangement of molybdenum (Mo) and sulfur (S) atoms sandwiched to form an S-Mo-S structure. These monolayers can be stacked in different configurations to form different polytypes of multilayer  $\text{MoS}_2$ . Previous studies on the most common configurations, the 2H (hexagonal) and 3R (rhombohedral) phases, reveal that stacking order is vital in various applications like piezoelectricity, nonlinear optics, and catalytic activity.[19–21] Similarly, structural defects in  $\text{MoS}_2$ , such as vacancies, substitu-

tions, dislocations, grain boundaries, and edges, can significantly influence its properties due to their impact on the atomic structure and electronic behavior.[11, 18, 22, 23] However, depending on the targeted application, their impact can be either detrimental or beneficial. For example, the mobility of carriers in electronic devices can get reduced by the collision with defects. In contrast, the presence of defects can enhance the performance of MoS<sub>2</sub> in various fields, including catalysis, energy storage, and sensing.[17]

Understanding the effect of stacking order and structural defects on thermal transport in MoS<sub>2</sub> is crucial for optimizing its thermal properties and thermoelectric applications and designing efficient thermal management strategies in various applications. Thermal conductivity of monolayer and multilayer MoS<sub>2</sub> in its suspended and substrate-bound form has been reported.[24–27] However, most of these works does not account for the possibility of structural defects or difference in the stacking order of MoS<sub>2</sub> crystals. Recently there have been theoretical studies on the thermal transport in MoS<sub>2</sub> with various defects like grain boundaries, vacancies, and substitutions.[28–35] A recent experimental work explored the phonon thermal transport in few-layer MoS<sub>2</sub> flakes with various point defect concentrations enabled by helium ion (He<sup>+</sup>) irradiation[36]. They observed that Mo vacancies significantly reduce the thermal conductivity of few-layer MoS<sub>2</sub> compared to S vacancies. Similarly, recent work on thermal transport in CVD-grown monolayer MoS<sub>2</sub> with grain boundaries also showed a lower thermal conductivity of the sample.[37]

In this letter, we report a systematic study of thickness-dependent thermal transport in supported MoS<sub>2</sub> crystals with intrinsic sulfur vacancies, including the 2H and 3R stacked bilayers. The in-plane thermal conductivity ( $\kappa$ ) and total interface conductance per unit area ( $g$ ) across the 2D material-substrate interface are obtained using Raman thermometry. For this, the first-order temperature coefficients of the intra-layer and inter-layer Raman modes are estimated. As per our understanding, this is the first report on the evolution of first-order temperature coefficients of low-frequency interlayer Raman modes of MoS<sub>2</sub> with layer number. Experimental results show that the  $\kappa$  decreases as the layer number increases, whereas the  $g$  increases. Our results also demonstrate that the thermal conductivity is significantly suppressed by sulfur vacancies in monolayer MoS<sub>2</sub>. However, this reduction in  $\kappa$  becomes less evident as the layer number increases. Hence our results confirm the recent theoretical predictions that the suppression of thermal transport in MoS<sub>2</sub> by point defects is more prominent in monolayers and becomes negligible as layer number increases. No

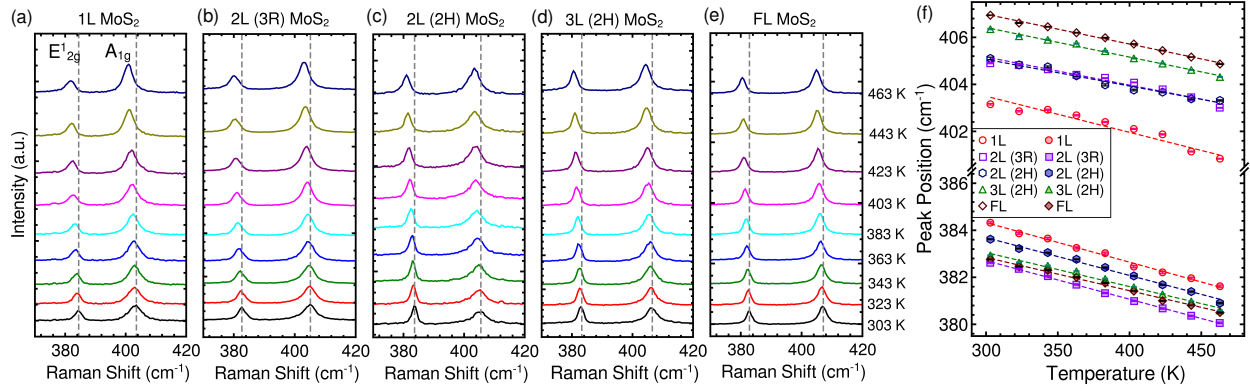


FIG. 1. (color online). The high frequency range of the Raman spectrum acquired at different temperatures using 532 nm excitation wavelength for (a) mono-, (b-c) bi-, (d) tri- and (e) few-layer MoS<sub>2</sub> crystals exfoliated on Si/SiO<sub>2</sub> substrate. The dashed (-) vertical lines indicates the position of E<sub>2g</sub><sup>1</sup> and A<sub>1g</sub> modes at 303 K. (f) The peak position of the A<sub>1g</sub> and E<sub>2g</sub><sup>1</sup> phonon modes at different temperatures for mono-, bi-, tri-, and few-layer MoS<sub>2</sub> crystals. The dashed (-) lines represent linear fit to data points.

significant variation is observed in the  $\kappa$  and  $g$  values of 2H and 3R stacked bilayer MoS<sub>2</sub> samples.

## RESULTS AND DISCUSSIONS

The 2D crystals of MoS<sub>2</sub> samples are prepared from bulk crystal by mechanical exfoliation and transferred on silicon wafers covered by 285 nm thick SiO<sub>2</sub>. The numbers of MoS<sub>2</sub> layers are first identified by optical contrast and then confirmed by Raman spectroscopy. The stacking order of bi- and trilayer samples is determined using interlayer phonon modes in their Raman spectra. The stoichiometry of the molybdenum disulfide (Mo:S ratio) is obtained in the range of 1:1.71 to 1:1.76 from the Scanning Electron Microscopy Energy Dispersive Spectroscopy (SEM-EDS) and X-ray Photoelectron Spectroscopy (XPS) measurement which confirms the presence of sulfur vacancies in the sample. Previous works also identified sulphur vacancy as the dominant category of defects in mechanically exfoliated MoS<sub>2</sub> samples.[38] For additional experimental details, see the supplementary information file. The thermal transport properties of 2D crystals of MoS<sub>2</sub> are measured using Raman thermometry.[39] This method benefits from its non-contact and non-destructive nature and

relatively simple implementation. The experiment involves the application of a localized heat source to the material and measuring the resulting temperature changes. Later a steady-state heat conduction model is used to extract the  $\kappa$  and  $g$  values of the 2D materials bound to a substrate.

Initially, a low-power laser beam is used to acquire the Raman spectrum of uniformly heated MoS<sub>2</sub> samples at different temperatures. The Figure 1 (a)-(e) represents the Raman spectra of MoS<sub>2</sub> samples recorded at different temperatures. The peaks around 384 cm<sup>-1</sup> and 406 cm<sup>-1</sup> correspond to the intralayer E<sub>2g</sub><sup>1</sup> and A<sub>1g</sub> modes, respectively. The E<sub>2g</sub><sup>1</sup> mode originates from the in-plane vibrations of the molybdenum (Mo) and sulfur (S) atoms, and the A<sub>1g</sub> mode originates from the out-of-plane vibrations of S atoms.[40] The variation in peak position with temperature is displayed in Figure 1(f). In all samples, the Raman mode frequency redshifts with increased temperature. This observed redshift in phonon frequency is mainly due to the contribution from thermal expansion and anharmonic effects at higher temperatures.[25] The data points are fitted with a linear function ( $\omega(T) = \omega_0 + \chi_T \times T$ ) to determine the first-order temperature coefficient ( $\chi_T$ ) of each phonon mode. The comparison of first-order temperature coefficient of E<sub>2g</sub><sup>1</sup> and A<sub>1g</sub> modes of MoS<sub>2</sub> flakes with different layer number and stacking order is provided in the Section S3 of the supporting information file. For all layer numbers and stacking orders under study, the magnitude of  $\chi_T$  value of E<sub>2g</sub><sup>1</sup> mode is higher than that of A<sub>1g</sub> mode which agrees with previous reports.[25, 41] This difference in temperature coefficients between the E<sub>2g</sub><sup>1</sup> and A<sub>1g</sub> Raman modes in MoS<sub>2</sub> can be attributed to their different symmetries and vibrational characteristics. Since the E<sub>2g</sub><sup>1</sup> mode corresponds to the in-plane vibration of S and Mo atoms, it is particularly sensitive to the thermal expansion and anharmonic effects in the in-plane direction, contributing to its higher temperature coefficient. We observed that the  $\chi_T$  values of the E<sub>2g</sub><sup>1</sup> mode exhibited a monotonous decrease in its magnitude as the layer number increased, whereas that of the A<sub>1g</sub> mode exhibited a sharp reduction from monolayer to bilayer and then increased with layer number.

Other than E<sub>2g</sub><sup>1</sup> and A<sub>1g</sub> modes, the Raman spectrum of MoS<sub>2</sub> samples contains interlayer phonon modes that appear in the low-frequency range (below 50 cm<sup>-1</sup>). Shear mode (SM) and layer breathing mode (LBM) originate from in-plane and out-of-plane vibrations of both S and Mo atoms, respectively, as shown in Figure 2(a). These modes are absent in the monolayer. The temperature coefficients of these interlayer modes in MoS<sub>2</sub> are not

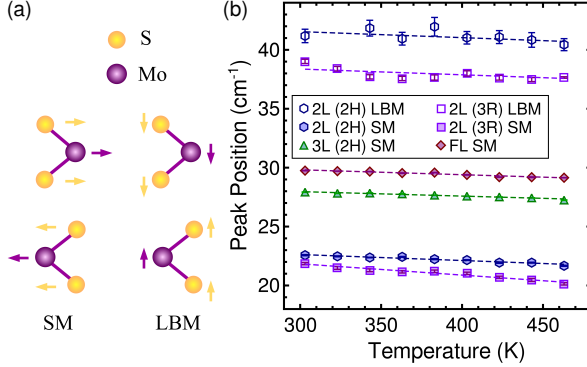


FIG. 2. (color online). (a) The peak position of the layer breathing mode (LBM) and shear mode (SM) at different temperatures for bi-, tri-, and few-layer MoS<sub>2</sub> crystals exfoliated on Si/SiO<sub>2</sub> substrate. (X and Y axis in linear scale). The dashed (-) lines represent linear fit to data points. (b) Schematic of the interlayer vibrational modes of MoS<sub>2</sub>

extensively studied as other Raman modes, primarily due to their relatively weaker intensity and the requisite of a more complex experimental setup with access to ultra-low frequencies and better spectral resolution.[41, 42] Here, we analyze the temperature dependence of low-frequency Raman modes of bi-, tri- and few-layer MoS<sub>2</sub> flakes. Figure 2(b) displays the variation in the peak position of low-frequency modes as a function of temperature. Both shear and layer breathing modes show redshift due to anharmonicity and increased interlayer separation at higher temperatures.[42] The temperature coefficients of low-frequency modes are given in Table SI. The  $\chi_T$  values of interlayer modes are much smaller than that of the high-frequency intralayer modes. The  $\chi_T$  value of the shear mode reduces their magnitude as the layer number increases.

Since both the E<sub>2g</sub><sup>1</sup> and A<sub>1g</sub> modes have higher temperature coefficients, it allows the measurement of the local temperature rise of the supported MoS<sub>2</sub> crystals due to a change in incident laser power by employing changes in the phonon frequency. Raman measurements are performed with different laser power for two different spot-size objectives. The incident power is measured with a power meter, and the absorbed power is calculated by considering the layer number-dependent optical absorption for the 532 nm wavelength. The variation of the peak position of E<sub>2g</sub><sup>1</sup> and A<sub>1g</sub> phonon modes with absorbed laser power is displayed in Figure 3. For all samples, the peak position redshifts with increased absorbed laser power. The fitting of data points with a linear function gives the power coefficient ( $d\omega/dP = \chi_p$ )

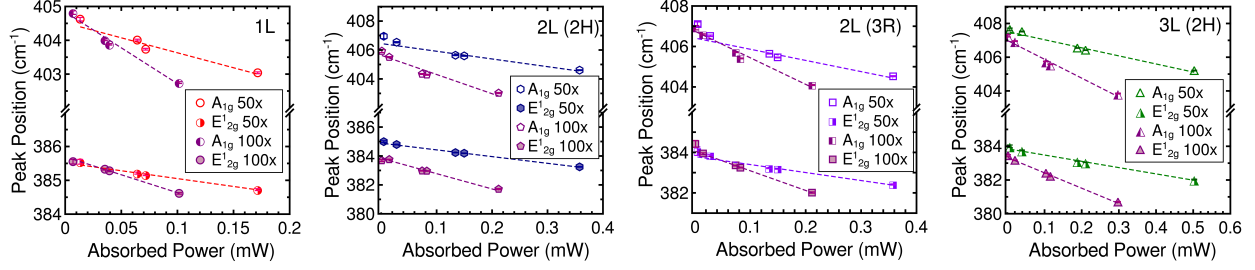


FIG. 3. (color online). The peak position of the  $A_{1g}$  and  $E_{2g}^1$  phonon modes at different absorbed laser power for bi- and tri-layer MoS<sub>2</sub> crystals exfoliated on Si/SiO<sub>2</sub> substrate. (X and Y axis in linear scale). The dashed (-) lines represent linear fit to data points.

of each Raman mode. The  $\chi_p$  of the  $A_{1g}$  mode appears more sensitive to variations in layer number than that of the  $E_{2g}^1$  mode. Since the  $A_{1g}$  mode is insensitive to in-plane strain and its power coefficient is more sensitive to layer number, the temperature-induced softening of the  $A_{1g}$  phonon mode is used to estimate local temperature rise and extract the thermal parameters.

Modeling of thermal transport in supported 2D materials subjected to laser heating has been reported previously[39, 43, 44]. Under the steady-state condition, laser-induced heating is compensated by the heat flow towards the low-temperature heat sink. By assuming diffusive phonon transport, the heat conduction equation for a supported 2D material can be written as [39]

$$\frac{1}{r} \frac{d}{dr} \left( r \frac{dT(r)}{dr} \right) - \frac{g}{\kappa t} (T(r) - T_a) + \frac{q_0''}{\kappa t} \exp\left(-\frac{r^2}{r_0^2}\right) = 0 \quad (1)$$

where  $T_a$  is the temperature of the substrate,  $t$  is the thickness of the 2D material, and  $q_0''$  is the peak absorbed laser power per unit area at the center of the beam. The absorbed laser power  $Q = q_0'' \pi r_0^2$  where  $r_0$  is the laser beam radius. Laser beam radius for 50x and 100x objectives is measured using Modified Knife edge method[45] and the values are 0.495  $\mu\text{m}$  and 0.297  $\mu\text{m}$ , respectively. Details of laser beam size measurement is included in Section S5 of the supporting information. The local temperature rise in the 2D crystal is defined as  $\Theta(r) = T(r) - T_a$ , and the average temperature rise is given by

$$\Theta_m(\kappa_s, g, r_0, Q) = \frac{\int_0^\infty \Theta(r) \exp\left(-\frac{r^2}{r_0^2}\right) r dr}{\int_0^\infty \exp\left(-\frac{r^2}{r_0^2}\right) r dr} \quad (2)$$

The thermal resistance which impedes the flow of heat in the system is obtained as  $R_m = \Theta_m/Q$ . The ratio of  $R_m$  for two distinct laser beam sizes depends only on the material parameters  $\kappa$  and  $g$ . Hence on solving Equation (1) for two beam sizes, we are able to estimate  $\kappa$  and  $g$  uniquely. The estimated in-plane thermal conductivity and interface conductance values, along with the  $R_m$  ratios, are presented in Table SII. The in-plane thermal conductivity decreases as the layer number increases, whereas the total interface conductance per unit area across the 2D material-substrate interface increases. The reduction in in-plane thermal conductivity for increased layer number is primarily attributed to the intrinsic scattering mechanism of phonons.[46]

TABLE I. Thermal resistance ratio, in-plane thermal conductivity and interface thermal conductance (at room-temperature) of mono-, bi- and tri-layer MoS<sub>2</sub> crystals on SiO<sub>2</sub>/Si substrate

Sample	$R_m$ ratio	$\kappa$ (W/mK)	$g$ (MW/m <sup>2</sup> K)
1L	$2.282 \pm 0.037$	$40 +8/-6$	$1.02 \pm 0.03$
2L (2H)	$2.137 \pm 0.084$	$33 +10/-7$	$1.09 +0.04/-0.05$
2L (3R)	$2.15 \pm 0.13$	$32 +13/-10$	$1.07 +0.13/-0.15$
3L (2H)	$2.082 \pm 0.068$	$28 \pm 6$	$1.23 \pm 0.05$

In this work, the measured value of  $\kappa$  of the monolayer MoS<sub>2</sub> sample is less than the previously reported value of  $55 \pm 20$  W/mK in samples without any structural defects.[26] However, in the case of bilayer samples, our measured value of  $\kappa$  is close to their reported value of  $35 \pm 7$  W/mK.[26] The reduction in the measured  $\kappa$  value of 1L MoS<sub>2</sub> can be attributed to the suppression of thermal conductivity by sulfur vacancies and this reduction in  $\kappa$  becomes less evident as the layer number increases. Our observations are in agreement with the recent theoretical predictions that the presence of sulfur vacancies significantly suppresses the thermal conductivity of monolayer MoS<sub>2</sub> due to the strong localization and increased scattering of phonons by defects.[31, 33] However, the thermal conductivity of bulk MoS<sub>2</sub> is expected to be less dependent on the presence of sulfur vacancies.[33]. Additionally, no significant variation is observed in the  $\kappa$  and  $g$  values of 2H and 3R stacked bilayer MoS<sub>2</sub> samples. It is also worth noting that the specific impact of sulfur vacancies on thermal transport in MoS<sub>2</sub> can depend on additional factors such as vacancy type, concentration and distribution.

## CONCLUSIONS

In conclusion, we investigated the first-order temperature coefficients of interlayer and intralayer Raman modes of MoS<sub>2</sub> crystals with inherent sulfur vacancies exfoliated on Si/SiO<sub>2</sub> substrate. Later the  $\kappa$  and  $g$  values of mono-, bi-, and tri-layer MoS<sub>2</sub> crystals are measured using Raman thermometry. The  $\kappa$  value decreases, and the  $g$  value decreases as the layer number increases. Importantly, we observed that the thermal conductivity is significantly suppressed by sulfur vacancies in monolayer MoS<sub>2</sub>. However, this reduction in  $\kappa$  becomes less evident as the layer number increases. Our results confirm previous theoretical predictions that the suppression of thermal transport in MoS<sub>2</sub> by point defects is more prominent in monolayers and becomes negligible as layer number increases. No significant variation is observed in the  $\kappa$  and  $g$  values of 2H and 3R stacked bilayer MoS<sub>2</sub> samples.

The authors thank the Central Instrumentation Facility (CIF) and Central Micro-Nano Fabrication Facility (CMFF), Indian Institute of Technology Palakkad and Central Instrumentation Facility (CIF) IISER Thiruvananthapuram for the experimental facilities.

## SUPPORTING INFORMATION

### S1. LAYER NUMBER AND STACKING ORDER

Raman measurements are carried out in a HORIBA LabRAM HR Evolution Raman spectrophotometer setup using an Nd-YAG laser of wavelength 532 nm off-resonance excitation and grating of 1800 lines/mm. All the Raman modes are fitted with Lorentzian function to extract spectral parameters. The relative separation of  $E_{2g}^1$  mode to  $A_{1g}$  mode increases as the layer number increases for the first few-layers.

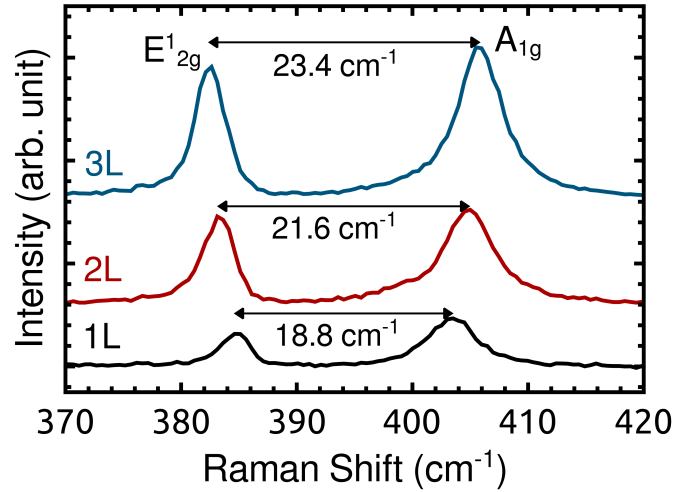


FIG. 4. High-frequency  $A_{1g}$  and  $E_{2g}^1$  Raman modes and their relative separation for mono-, bi- and tri-layer  $\text{MoS}_2$

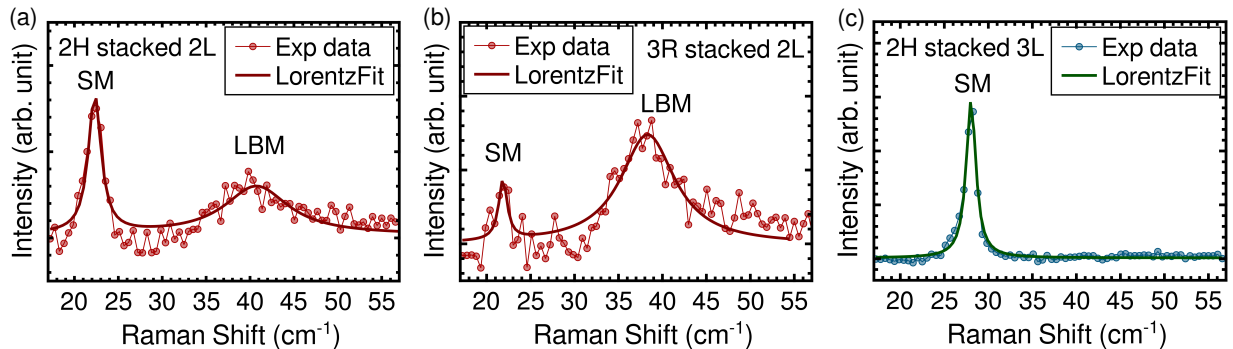


FIG. 5. Low-frequency shear mode and layer breathing mode of (a) 3R stacked bilayer (b) 2H stacked bilayer and (c) 2H stacked trilayer  $\text{MoS}_2$

The position of shear mode for bilayer and trilayer  $\text{MoS}_2$  is  $\sim 22 \text{ cm}^{-1}$  and  $\sim 28 \text{ cm}^{-1}$ , respectively. The 3R polytype has lower frequency of the layer breathing mode compared to 2H polytype and is mainly due to the lower interlayer coupling strength in 3R stacking.[47] Additionally, the integrated intensity ratios of the layer breathing mode (LBM) to the shear mode (SM) strongly depends on the stacking order and interlayer interaction strength.  $I(\text{LBM})/I(\text{SM})$  of 3R polytype is nearly 5-6 times that of the 2H polytype.

## S2. STOICHIOMETRY DETERMINATION

SEM-EDS mapping performed on different multilayer flakes on the  $\text{Si}/\text{SiO}_2$  substrate. XPS measurement carried out with  $\sim 6 \text{ mm}$  diameter  $\text{Mg K}\alpha$  radiation (1253.6eV).

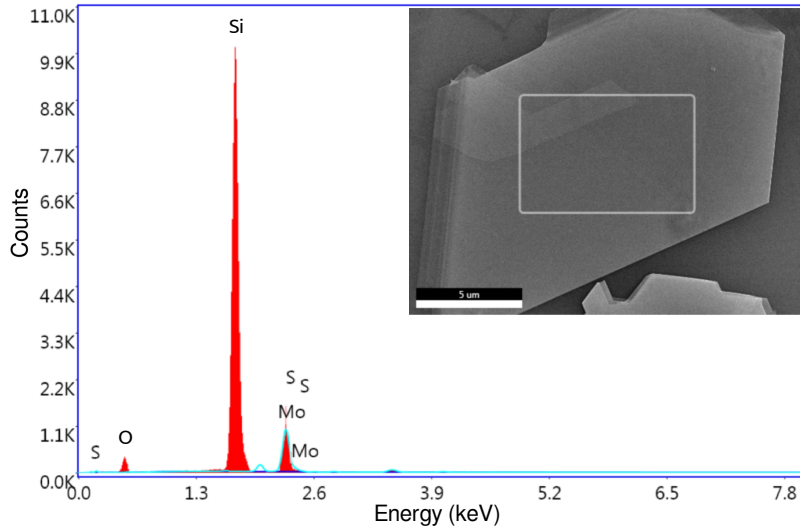


FIG. 6. EDS mapping data of  $\text{MoS}_2$  flake on  $\text{Si}/\text{SiO}_2$  substrate. Mapped area is marked in white rectangle.

## S3. RAMAN MEASUREMENTS AND THERMOMETRY

For all temperature-dependent measurements, excitation laser power is kept below 200  $\mu\text{W}$  to avoid local heating. To perform measurements at higher temperatures a Linkam HFS600E-PB4 temperature-controller stage is used. Raman measurements are performed over the spectral range of  $10\text{-}600 \text{ cm}^{-1}$ . All laser power dependent measurements are carried out using a step variable neutral density filter at ambient conditions.

### S3. 1. Temperature coefficient of high-frequency Raman modes

The FWHM and first-order temperature coefficient of high frequency Raman modes obtained for different samples are summarized in Figure 7. The  $\chi_T$  value of 2H and 3R stacked bilayer MoS<sub>2</sub> matches well.

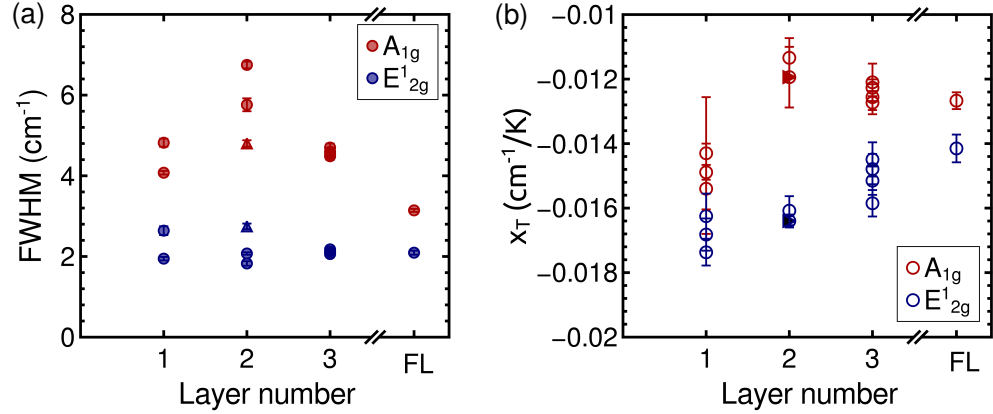


FIG. 7. The value of (a) FWHM and (b) first-order temperature coefficient of  $E_{2g}^1$  and  $A_{1g}$  modes for mono-, bi-, tri- and few-layer MoS<sub>2</sub> crystals on Si/SiO<sub>2</sub> substrate. Different data points indicate different samples and triangles indicate 3R stacked bilayer.

### S3. 2. Temperature coefficient of low-frequency Raman modes

The first-order temperature coefficients of low frequency Raman modes obtained for different samples are summarized in Table SI. The  $\chi_T$  values of shear modes of 2H stacked bilayer is much smaller than that of 3R stacked bilayer. This variation can be attributed to the difference in the coupling strength of near by layers in different stacking configurations. For trilayer samples both SM and LBM has the same phonon frequency. The temperature coefficient of layer breathing mode and higher orders of low-frequency modes of few-layer samples are not obtained due to less access to ultra-low frequencies.

TABLE SI. Temperature coefficients of Low-frequency interlayer modes of bi-, tri and few-layer MoS<sub>2</sub> crystals on SiO<sub>2</sub>/Si substrate

Sample	First-order temperature coefficient $\chi_T$ , (cm <sup>-1</sup> /K)	
	Shear mode (SM)	Layer breathing mode (LBM)
2L (3R) MoS <sub>2</sub>	-0.00956 ± 0.00082	-0.0049 ± 0.0018
2L (2H) MoS <sub>2</sub>	-0.00506 ± 0.00046	-0.0051 ± 0.0027
3L (2H) MoS <sub>2</sub>	-0.00411 ± 0.00055	
FL MoS <sub>2</sub>	-0.00417 ± 0.00030	

In 3R polytype the observed temperature coefficient of layer breathing mode is smaller than that of shear mode. This might be due to the absence of contribution from thermal expansion in layer breathing mode.

### S3. 3. Laser power dependent Raman measurements

The power coefficients of  $E_{2g}^1$  mode is less sensitive to variations in layer number. The magnitude of power coefficient of  $E_{2g}^1$  and  $A_{1g}$  Raman mode decreases with layer number as given in Figure 8.

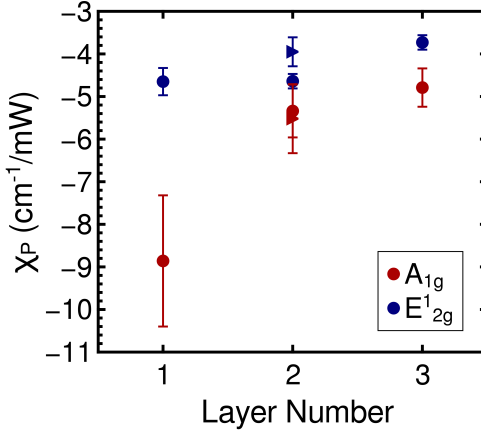


FIG. 8. The value of power coefficient of  $E_{2g}^1$  and  $A_{1g}$  modes for mono-, bi- and tri-layer MoS<sub>2</sub> crystals on Si/SiO<sub>2</sub> substrate measured using 50x objective with 495  $\mu\text{m}$  beam size. Triangles indicate 3R stacked bilayer.

## S4. THERMAL TRANSPORT MODELLING AND ESTIMATION OF $\kappa$ AND $g$

### S4. 1. Heat conduction model

A laser beam with Gaussian intensity distribution is used for local heating of the sample. Under steady-state the local heating is compensated by the conduction of heat to surrounding. The differential equation in cylindrical coordinates corresponding to heat diffusion in the 2D material and across the 2D material-substrate interface is[39]

$$\frac{1}{r} \frac{d}{dr} \left( r \frac{dT(r)}{dr} \right) - \frac{g}{\kappa t} (T(r) - T_a) + \frac{q_0''}{\kappa t} \exp\left(-\frac{r^2}{r_0^2}\right) = 0 \quad (3)$$

The temperature distribution  $T(r)$  in the plane of 2D material has radial symmetry and Gaussian profile. Through out the thickness ( $t$ ) of the 2D material same temperature profile is assumed. The substrate is assumed to be at ambient temperature ( $T_a$ ) and acts as a heat

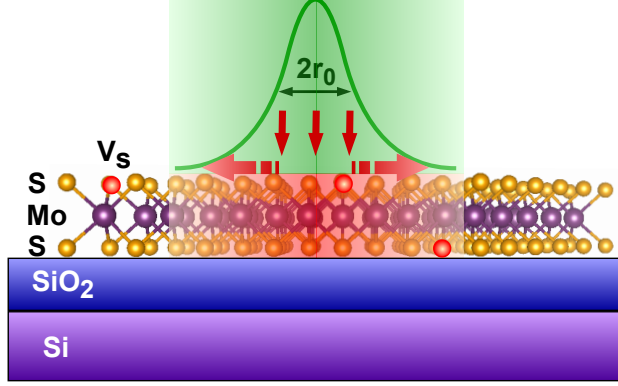


FIG. 9. (a) Schematic of the laser heating and thermal transport in MoS<sub>2</sub> with sulfur vacancies exfoliated on Si/SiO<sub>2</sub> substrate.

sink. The temperature rise in the 2D crystal is defined as  $\Theta(r) = T(r) - T_a$ , and the average temperature rise is given by

$$\Theta_m(\kappa_s, g, r_0, Q) = \frac{\int_0^\infty \Theta(r) \exp\left(-\frac{r^2}{r_0^2}\right) r dr}{\int_0^\infty \exp\left(-\frac{r^2}{r_0^2}\right) r dr} \quad (4)$$

where  $Q = q_0'' \pi r_0^2$  is the total absorbed power and  $r_0$  is the laser beam radius. The thermal resistance is defined as  $R_m = \Theta_m/Q$ . The optical absorption coefficients of mono-, bi- and tri-layer samples are taken as 5.8%, 12.1% and 17%, respectively. The layer thickness of mono-, bi- and tri-layer samples used for the calculations are 0.65 nm, 1.4 nm and 2.4 nm, respectively. Since the convection through air accounts for less than 0.15% of the total heat conduction, its effect is ignored in the estimation of thermal parameters.[26]

#### S4. 2. Estimation of $\kappa$ and $g$

To determine the in-plane thermal conductivity ( $\kappa$ ) and the interface conductance per unit area across the 2D material-substrate interface ( $g$ ), we used the boundary conditions proposed by Cai et al.[39] and solved Equation (4) using numerical integration; Estimated parameters are given in Table I in the manuscript.

To confirm further thermal parameters are calculated by using the boundary conditions and analytical solution proposed by Goushehgir [44]; Estimated parameters are given in Table SII. These values are in good agreement with the values obtained from numerical

integration. When  $\text{MoS}_2$  is supported on a substrate with a silicon dioxide ( $\text{SiO}_2$ ) top layer, the interfacial thermal resistance at the  $\text{MoS}_2$ -substrate interface can become a significant factor in determining the overall thermal conductivity of the system.

TABLE SII. In-plane thermal conductivity and interface thermal conductance (at room-temperature) of  $\text{MoS}_2$  crystals

Sample	$\kappa$ (W/mK)	$g$ (MW/m <sup>2</sup> K)
1L	40 +8/-6	1.02 $\pm$ 0.03
2L (2H)	33 +10/-7	1.09 +0.04/-0.05
2L (3R)	32 +13/-10	1.07 +0.13/-0.15
3L (2H)	28 $\pm$ 6	1.23 $\pm$ 0.05

### S4. 3. Layer number and stacking order dependence of thermal properties

Variation of thermal parameters with layer number and stacking order given in Figure 10.

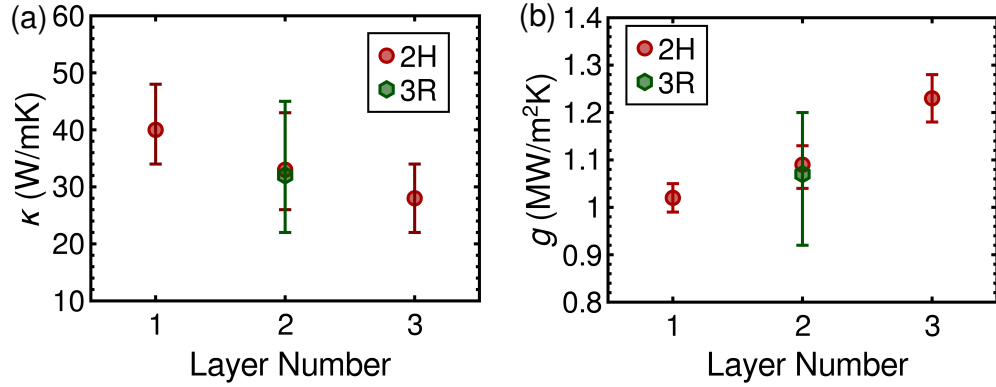


FIG. 10. Variation of (a) in-plane thermal conductivity and (b) total interface thermal conductance of  $\text{MoS}_2$  with layer number and stacking order

### S4. 4. Substrate heating

Variation of Si peak position with stage temperature and laser power is given in Figure 11 (a) and (b). No measurable shift in Si peak position is observed in the local laser heating. Due to high specific heat of  $\text{SiO}_2$  layer it acts as a good heat sink and results in negligible heating of  $\text{SiO}_2$  and underlying Si.

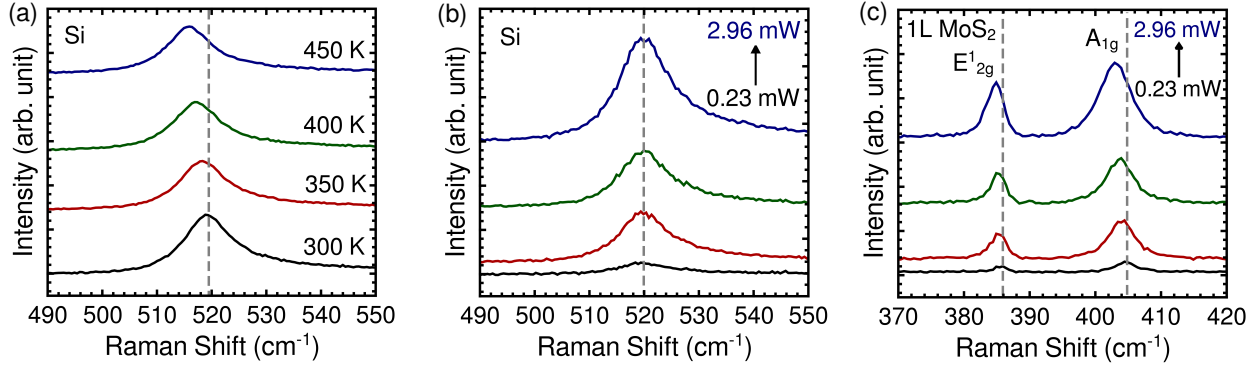


FIG. 11. The variation of Silicon peak position with (a) temperature and (b) absorbed power for monolayer MoS<sub>2</sub> on Si/SiO<sub>2</sub> substrate. (c) The variation of high-frequency Raman modes of monolayer MoS<sub>2</sub> on Si/SiO<sub>2</sub> substrate. The power values given in the plots corresponds to the power absorbed by monolayer MoS<sub>2</sub>.

## S5. LASER BEAM SIZE DETERMINATION

The laser beam radius ( $r_0$ ) is defined as the distance from the center of the beam at which intensity reduces to  $1/e$  times its peak value. Laser beam size for both 50x and 100x objectives are measured by modified knife-edge method.[45] A thin film of gold with sharp-edges is deposited on a Si/SiO<sub>2</sub> substrate. Linear Raman mapping is performed across the sharp edge of the gold film to detect the Raman signal of silicon. The acquisition time set as 2s, accumulations 2 and spectral range 420 cm<sup>-1</sup> to 600 cm<sup>-1</sup>. Figure 12 (a) shows the laser beam spot size measurement set-up and the optical image of the sharp edge. Figure 12 (b) shows the normalized intensity profile of the Si peak at different locations across the sharp edge measured using 50x and 100x objectives. The normalized intensity profile is fitted with the function:

$$I(x) = \frac{I_0}{2} \left( 1 + \operatorname{erf} \left( \frac{x - x_0}{w} \right) \right) \quad (5)$$

The fitted normalized intensity profile is differentiated with respect to the distance x. The  $dI/dx$  data has a Gaussian behavior with a functional form  $A \cdot \exp \left( -\frac{(x-x_0)^2}{w^2} \right)$ . Since the source term in the heat conduction equation has the form  $\exp \left( -\frac{r^2}{r_0^2} \right)$ , the  $w$  value can be identified as the laser beam radius,  $r_0$ . The measurements are repeated and the mean value for each objective is used for the estimation of thermal transport parameters.

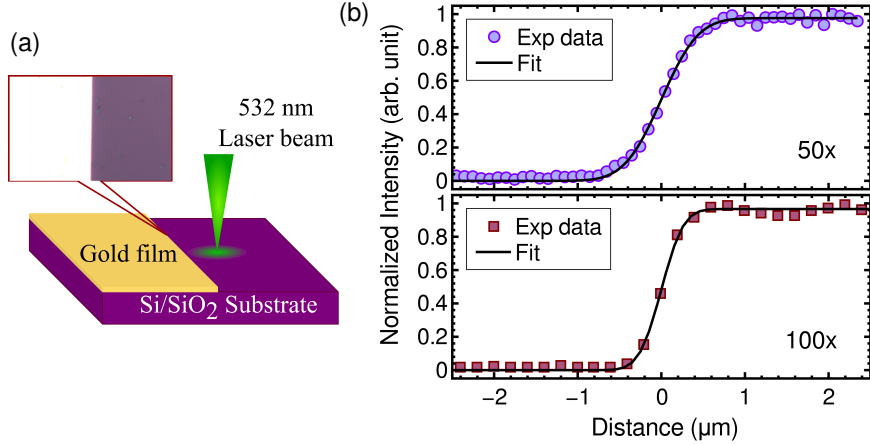


FIG. 12. (a) Schematic of the laser beam size measurement set-up (optical image of the sharp edge given in inset). (b) The normalized intensity profile of the Si peak at different locations across the sharp edge measured using 50x and 100x objectives. The line represents the fit using Equation (5)

\* ranjuna.mk@gmail.com

† jayakumar@iitpkd.ac.in

- [1] K. F. Mak, C. Lee, J. Hone, J. Shan, and T. F. Heinz, Atomically thin mos 2: a new direct-gap semiconductor, *Physical review letters* **105**, 136805 (2010).
- [2] X. Liu, T. Galfsky, Z. Sun, F. Xia, E.-c. Lin, Y.-H. Lee, S. Kéna-Cohen, and V. M. Menon, Strong light–matter coupling in two-dimensional atomic crystals, *Nature Photonics* **9**, 30 (2015).
- [3] D. Xiao, G.-B. Liu, W. Feng, X. Xu, and W. Yao, Coupled spin and valley physics in monolayers of mos 2 and other group-vi dichalcogenides, *Physical review letters* **108**, 196802 (2012).
- [4] K. F. Mak, K. He, J. Shan, and T. F. Heinz, Control of valley polarization in monolayer mos2 by optical helicity, *Nature nanotechnology* **7**, 494 (2012).
- [5] H. Zeng, J. Dai, W. Yao, D. Xiao, and X. Cui, Valley polarization in mos2 monolayers by optical pumping, *Nature nanotechnology* **7**, 490 (2012).
- [6] P. Chakrabarti, F. Mujeeb, and S. Dhar, Enhancement of valley polarization in cvd grown monolayer mos2 films, *Applied Physics Letters* **121**, 072103 (2022).

[7] M. Buscema, M. Barkelid, V. Zwiller, H. S. van der Zant, G. A. Steele, and A. Castellanos-Gomez, Large and tunable photothermoelectric effect in single-layer mos2, *Nano letters* **13**, 358 (2013).

[8] J. Wu, H. Schmidt, K. K. Amara, X. Xu, G. Eda, and B. Ozyilmaz, Large thermoelectricity via variable range hopping in chemical vapor deposition grown single-layer mos2, *Nano letters* **14**, 2730 (2014).

[9] H. Huang, Y. Cui, Q. Li, C. Dun, W. Zhou, W. Huang, L. Chen, C. A. Hewitt, and D. L. Carroll, Metallic 1t phase mos2 nanosheets for high-performance thermoelectric energy harvesting, *Nano Energy* **26**, 172 (2016).

[10] B. Radisavljevic, A. Radenovic, J. Brivio, V. Giacometti, and A. Kis, Single-layer mos2 transistors, *Nature nanotechnology* **6**, 147 (2011).

[11] Y. Chen, S. Huang, X. Ji, K. Adeppali, K. Yin, X. Ling, X. Wang, J. Xue, M. Dresselhaus, J. Kong, *et al.*, Tuning electronic structure of single layer mos2 through defect and interface engineering, *ACS nano* **12**, 2569 (2018).

[12] R. Cheng, S. Jiang, Y. Chen, Y. Liu, N. Weiss, H.-C. Cheng, H. Wu, Y. Huang, and X. Duan, Few-layer molybdenum disulfide transistors and circuits for high-speed flexible electronics, *Nature communications* **5**, 5143 (2014).

[13] M. Fontana, T. Deppe, A. K. Boyd, M. Rinzan, A. Y. Liu, M. Paranjape, and P. Barbara, Electron-hole transport and photovoltaic effect in gated mos2 schottky junctions, *Scientific reports* **3**, 1 (2013).

[14] T. Pham, G. Li, E. Bekyarova, M. E. Itkis, and A. Mulchandani, Mos2-based optoelectronic gas sensor with sub-parts-per-billion limit of no2 gas detection, *ACS nano* **13**, 3196 (2019).

[15] M. Bernardi, M. Palummo, and J. C. Grossman, Extraordinary sunlight absorption and one nanometer thick photovoltaics using two-dimensional monolayer materials, *Nano letters* **13**, 3664 (2013).

[16] L. Sun, C.-Y. Wang, A. Krasnok, J. Choi, J. Shi, J. S. Gomez-Diaz, A. Zepeda, S. Gwo, C.-K. Shih, A. Alù, *et al.*, Separation of valley excitons in a mos2 monolayer using a subwavelength asymmetric groove array, *Nature Photonics* **13**, 180 (2019).

[17] J. Xu, G. Shao, X. Tang, F. Lv, H. Xiang, C. Jing, S. Liu, S. Dai, Y. Li, J. Luo, *et al.*, Frenkel-defected monolayer mos2 catalysts for efficient hydrogen evolution, *Nature communications* **13**, 2193 (2022).

[18] H. Qiu, T. Xu, Z. Wang, W. Ren, H. Nan, Z. Ni, Q. Chen, S. Yuan, F. Miao, F. Song, *et al.*, Hopping transport through defect-induced localized states in molybdenum disulphide, *Nature communications* **4**, 2642 (2013).

[19] R. J. Toh, Z. Sofer, J. Luxa, D. Sedmidubský, and M. Pumera, 3r phase of mos2 and ws2 outperforms the corresponding 2h phase for hydrogen evolution, *Chemical Communications* **53**, 3054 (2017).

[20] J. Shi, P. Yu, F. Liu, P. He, R. Wang, L. Qin, J. Zhou, X. Li, J. Zhou, X. Sui, *et al.*, 3r mos2 with broken inversion symmetry: a promising ultrathin nonlinear optical device, *Advanced Materials* **29**, 1701486 (2017).

[21] H. Hallil, W. Cai, K. Zhang, P. Yu, S. Liu, R. Xu, C. Zhu, Q. Xiong, Z. Liu, and Q. Zhang, Strong piezoelectricity in 3r-mos2 flakes, *Advanced Electronic Materials* **8**, 2101131 (2022).

[22] W. Zhou, X. Zou, S. Najmaei, Z. Liu, Y. Shi, J. Kong, J. Lou, P. M. Ajayan, B. I. Yakobson, and J.-C. Idrobo, Intrinsic structural defects in monolayer molybdenum disulfide, *Nano letters* **13**, 2615 (2013).

[23] S. Tongay, J. Suh, C. Ataca, W. Fan, A. Luce, J. S. Kang, J. Liu, C. Ko, R. Raghunathanan, J. Zhou, *et al.*, Defects activated photoluminescence in two-dimensional semiconductors: interplay between bound, charged and free excitons, *Scientific reports* **3**, 2657 (2013).

[24] R. Yan, J. R. Simpson, S. Bertolazzi, J. Brivio, M. Watson, X. Wu, A. Kis, T. Luo, A. R. Hight Walker, and H. G. Xing, Thermal conductivity of monolayer molybdenum disulfide obtained from temperature-dependent raman spectroscopy, *ACS nano* **8**, 986 (2014).

[25] S. Sahoo, A. P. Gaur, M. Ahmadi, M. J.-F. Guinel, and R. S. Katiyar, Temperature-dependent raman studies and thermal conductivity of few-layer mos2, *The Journal of Physical Chemistry C* **117**, 9042 (2013).

[26] X. Zhang, D. Sun, Y. Li, G.-H. Lee, X. Cui, D. Chenet, Y. You, T. F. Heinz, and J. C. Hone, Measurement of lateral and interfacial thermal conductivity of single-and bilayer mos2 and mose2 using refined optothermal raman technique, *ACS applied materials & interfaces* **7**, 25923 (2015).

[27] P. Yuan, R. Wang, T. Wang, X. Wang, and Y. Xie, Nonmonotonic thickness-dependence of in-plane thermal conductivity of few-layered mos 2: 2.4 to 37.8 nm, *Physical Chemistry Chemical Physics* **20**, 25752 (2018).

[28] Z. Ding, Q.-X. Pei, J.-W. Jiang, and Y.-W. Zhang, Manipulating the thermal conductivity of

monolayer mos2 via lattice defect and strain engineering, *The Journal of Physical Chemistry C* **119**, 16358 (2015).

[29] B. Peng, Z. Ning, H. Zhang, H. Shao, Y. Xu, G. Ni, and H. Zhu, Beyond perturbation: role of vacancy-induced localized phonon states in thermal transport of monolayer mos2, *The Journal of Physical Chemistry C* **120**, 29324 (2016).

[30] D. Saha and S. Mahapatra, Theoretical insights on the electro-thermal transport properties of monolayer mos2 with line defects, *Journal of Applied Physics* **119**, 134304 (2016).

[31] Y. Wang, K. Zhang, and G. Xie, Remarkable suppression of thermal conductivity by point defects in mos2 nanoribbons, *Applied Surface Science* **360**, 107 (2016).

[32] C. Lin, X. Chen, and X. Zou, Phonon-grain-boundary-interaction-mediated thermal transport in two-dimensional polycrystalline mos2, *ACS applied materials & interfaces* **11**, 25547 (2019).

[33] C. A. Polanco, T. Pandey, T. Berlijn, and L. Lindsay, Defect-limited thermal conductivity in mos 2, *Physical Review Materials* **4**, 014004 (2020).

[34] K. Xu, T. Liang, Z. Zhang, X. Cao, M. Han, N. Wei, and J. Wu, Grain boundary and misorientation angle-dependent thermal transport in single-layer mos 2, *Nanoscale* **14**, 1241 (2022).

[35] A. J. Gabourie, S. V. Suryavanshi, A. B. Farimani, and E. Pop, Reduced thermal conductivity of supported and encased monolayer and bilayer mos2, *2D Materials* **8**, 011001 (2020).

[36] Y. Zhao, M. Zheng, J. Wu, X. Guan, A. Suwardi, Y. Li, M. Lal, G. Xie, G. Zhang, L. Zhang, *et al.*, Modification of thermal transport in few-layer mos 2 by atomic-level defect engineering, *Nanoscale* **13**, 11561 (2021).

[37] M. Yarali, X. Wu, T. Gupta, D. Ghoshal, L. Xie, Z. Zhu, H. Brahmi, J. Bao, S. Chen, T. Luo, *et al.*, Effects of defects on the temperature-dependent thermal conductivity of suspended monolayer molybdenum disulfide grown by chemical vapor deposition, *Advanced Functional Materials* **27**, 1704357 (2017).

[38] J. Hong, Z. Hu, M. Probert, K. Li, D. Lv, X. Yang, L. Gu, N. Mao, Q. Feng, L. Xie, *et al.*, Exploring atomic defects in molybdenum disulphide monolayers, *Nature communications* **6**, 6293 (2015).

[39] W. Cai, A. L. Moore, Y. Zhu, X. Li, S. Chen, L. Shi, and R. S. Ruoff, Thermal transport in suspended and supported monolayer graphene grown by chemical vapor deposition, *Nano letters* **10**, 1645 (2010).

- [40] H. Li, Q. Zhang, C. C. R. Yap, B. K. Tay, T. H. T. Edwin, A. Olivier, and D. Baillargeat, From bulk to monolayer mos2: evolution of raman scattering, *Advanced Functional Materials* **22**, 1385 (2012).
- [41] H. Kim, H. Ko, S. M. Kim, and H. Rho, Temperature dependent raman spectroscopy of shear and layer breathing modes in bilayer mos2, *Current Applied Physics* **25**, 41 (2021).
- [42] I. Maity, P. K. Maiti, and M. Jain, Temperature-dependent layer breathing modes in two-dimensional materials, *Physical Review B* **97**, 161406 (2018).
- [43] J. Judek, A. P. Gertych, M. Świniarski, A. Łapińska, A. Dużyńska, and M. Zdrojek, High accuracy determination of the thermal properties of supported 2d materials, *Scientific reports* **5**, 1 (2015).
- [44] S. H. Goushehgir, Simple exact analytical solution of laser-induced thermal transport in supported 2d materials, *International Communications in Heat and Mass Transfer* **128**, 105592 (2021).
- [45] A. Taube, J. Judek, A. Lapinska, and M. Zdrojek, Temperature-dependent thermal properties of supported mos2 monolayers, *ACS applied materials & interfaces* **7**, 5061 (2015).
- [46] E. Easy, Y. Gao, Y. Wang, D. Yan, S. M. Goushehgir, E.-H. Yang, B. Xu, and X. Zhang, Experimental and computational investigation of layer-dependent thermal conductivities and interfacial thermal conductance of one-to three-layer wse2, *ACS Applied Materials & Interfaces* **13**, 13063 (2021).
- [47] J. Van Baren, G. Ye, J.-A. Yan, Z. Ye, P. Rezaie, P. Yu, Z. Liu, R. He, and C. H. Lui, Stacking-dependent interlayer phonons in 3r and 2h mos2, *2D Materials* **6**, 025022 (2019).